



**HAL**  
open science

# Ectoderm to mesoderm transition by downregulation of actomyosin contractility

Leily Kashkooli, David Rozema, Lina Espejo-Ramirez, Paul Lasko, François Fagotto

► **To cite this version:**

Leily Kashkooli, David Rozema, Lina Espejo-Ramirez, Paul Lasko, François Fagotto. Ectoderm to mesoderm transition by downregulation of actomyosin contractility. 2019. hal-02332030v2

**HAL Id: hal-02332030**

**<https://hal.science/hal-02332030v2>**

Preprint submitted on 9 Dec 2019

**HAL** is a multi-disciplinary open access archive for the deposit and dissemination of scientific research documents, whether they are published or not. The documents may come from teaching and research institutions in France or abroad, or from public or private research centers.

L'archive ouverte pluridisciplinaire **HAL**, est destinée au dépôt et à la diffusion de documents scientifiques de niveau recherche, publiés ou non, émanant des établissements d'enseignement et de recherche français ou étrangers, des laboratoires publics ou privés.

# **Ectoderm to mesoderm transition by downregulation of actomyosin contractility**

**Leily Kashkooli<sup>1,2,3</sup>, David Rozema<sup>1,2,3</sup>, Lina Espejo-Ramirez<sup>1</sup>, Paul Lasko<sup>2</sup> and François Fagotto<sup>1,2,4</sup>**

<sup>1</sup>CRBM, University of Montpellier and CNRS, Montpellier 34293, France

and <sup>2</sup>Dept. of Biology, McGill University, Montreal, QC, Canada H3A1B1.

<sup>3</sup>These authors contributed equally to this work

<sup>4</sup>Correspondence to François Fagotto, email: francois.fagotto@crbm.cnrs.fr

## Summary

Collective migration of cohesive tissues is a fundamental process in morphogenesis, and is particularly well illustrated during gastrulation by the rapid and massive internalization of the mesoderm, which contrasts with the much more modest movements of the ectoderm. In the *Xenopus* embryo, the differences in morphogenetic capabilities of ectoderm and mesoderm can be connected to the properties of individual cells, which, when studied in vitro, show opposite intrinsic organizations, cohesive for ectoderm, dispersive for mesoderm. Surprisingly, we find these seemingly deep differences can be accounted for simply by differences in Rock-dependent actomyosin contractility. We show that Rock inhibition is sufficient to rapidly unleash motility in the ectoderm and confer it with mesoderm-like properties. In the mesoderm, this motility is dependent on two RhoA negative regulators, the small GTPase Rnd1 and the RhoGAP Shirin/Dlc2/ArhGAP37. Both are absolutely essential for gastrulation. At the cellular and tissue level, the two regulators show overlapping yet distinct functions. They both contribute to decrease cortical tension and confer motility, but Shirin tends to increase tissue fluidity and stimulate dispersion, while Rnd1 tends to favour more compact collective migration. Thus, each is able to contribute to a specific property of the migratory behaviour of the mesoderm.

## Introduction

The ability of tissues to dynamically rearrange is at the core of animal morphogenesis. One of the best examples is the internalization of the mesoderm during gastrulation. The mesoderm, which originates from the ectoderm through an inductive process, becomes actively migratory, moves inside the embryo, and colonizes the inner space between the overlying ectoderm and the central endoderm. On a first glance this behaviour appears related to the classical (EMT) observed for single metastatic cells escaping solid tumours. Yet, in many modes of gastrulation, the mesoderm cells move inside the embryo as a compact mass. This collective migration of the mesoderm is particularly striking in the amphibian model *Xenopus laevis*, where it is called involution<sup>1</sup>. Furthermore, the early *Xenopus* embryo is already multi-layered, and the mesoderm derives from the deep ectoderm layer, which does not display apical-basal polarity at the time of gastrulation. Thus, in this simple system, one can directly witness a tissue acquiring a migratory behaviour without loss of cell-cell adhesion or changes in polarity. We propose that this process, which we name the “ectoderm to mesoderm transition”, or “mesoderm transition” for short, constitutes a basal mode, which can teach us a great deal about the core cellular mechanisms that control tissue dynamicity.

The *Xenopus* embryo offers the unique possibility to easily dissect specific tissues, prepare explants and/or dissociate them into single cells, thus allowing the study of intrinsic cell and tissue properties in the absence of confounding influences of other surrounding embryonic structures. Importantly, the morphogenetic events occurring during *Xenopus* gastrulation are recapitulated in isolated explants, and furthermore, even individual dissociated cells have characteristics that clearly relate to the properties of the corresponding tissues: Ectoderm cells show higher cortical stiffness, higher cell-cell adhesion, and are largely immotile, while the softer mesoderm cells spread and migrate when laid on a fibronectin (FN) substrate<sup>2-5</sup>. Note that the mesoderm is composed of different regions along the anterior-posterior axis, sequentially the mesendoderm, the prechordal mesoderm, and the posterior chordal mesoderm. The two former regions form a single “motility domain”<sup>2,4</sup>, characterized by very active migration. The posterior chordal mesoderm, which is internalized at later stages of gastrulation, is much less migratory, and undergoes a particular movement, called convergent-extension<sup>4</sup>. In this study, we focus on the “migratory” mesoderm, which for the sake of simplicity is here referred to as “mesoderm”.

We have based this investigation of mesoderm transition on the hypothesis that the high cortical contractility of ectoderm cells may be prohibitive for motility, and that its decrease may be a key step in the mesoderm transition. We show indeed that inhibition of the Rho-Rock pathway is sufficient to confer ectoderm cells with migratory properties. We identify two mesoderm-specific negative regulators of RhoA, Rnd1 and Shirin (also called Dlc2, Stard13 or AhrGAP37), as absolutely required for gastrulation and more specifically for proper mesoderm migration, as predicted from our initial hypothesis. Our analysis of the impact of these regulators at the cell and tissue level supports a model where Rnd1 and Shirin cooperate toward a general downregulation of actomyosin contractility, allowing cells to become motile, but also have opposing activities, dispersive for Shirin and cohesive for Rnd1, which balance each other to produce the right physical properties for effective mesoderm involution.

## Results

### Distinct characteristics of ectoderm and mesoderm at the cell level

We first studied ectoderm and mesoderm cells *in vitro* in order to firmly characterize their basic intrinsic properties. Dissociated cells from early gastrula tissues were plated on fibronectin (FN) and imaged by live confocal microscopy. FN is the major extracellular matrix component in the gastrula, where it forms a sparse network<sup>6,7</sup>. Accordingly, we used low FN for all our assays. Ectoderm and mesoderm cells have radically different morphologies and behaviour: Ectoderm cells typically remain round and produce large blebs (Fig.1A,F)<sup>8</sup>, and they do not migrate (Fig.1G, suppl. Movie 1)<sup>2</sup>. On the contrary, mesoderm cells spread, form multiple prominent protrusions (Fig.1B, suppl. Movie 2) and migrate at high speed (Fig.1G)<sup>2</sup>. Single mesoderm cell migration typically has low persistence, with one of the extended lamellipodia rapidly commuted to the cell's tail (Fig.S1A)<sup>9</sup>. As a consequence, protrusive and retracting structures can be considered as oscillating states, unlike the strongly polarized extensions of many classical mesenchymal cell types.

The organization of matrix adhesions, marked by vinculin and paxillin, completely accounted for the differences in morphology and behaviour, as mesoderm cells displayed typical vinculin and paxillin-positive focal adhesions (FAs) (Fig.1B'). These FAs were rapidly remodelled during migration (Fig.1F'). Ectoderm cells showed a completely different organization, harboring a highly stereotypical ring-shaped vinculin and paxillin-rich structure (Fig.1A',F). These rings were immobile (Fig.1F, suppl. Movie 1). Note that mesoderm cells displayed a spectrum of protrusions, from large lamellipodia to thin extensions, which all showed vinculin and paxillin enriched structures (Fig.1D',F'). For simplicity, we will refer here to all the vinculin-rich structures detected on the ventral cell surface as FAs. Note also that in all subsequent experiments, we only tracked vinculin. Its absence did not preclude the occurrence of vinculin-negative FAs, but vinculin recruitment is an established parameter reflecting the tension exerted on adhesive structures<sup>10,11</sup>. We quantified the fraction of vinculin-Cherry detected on the ventral surface that concentrated at FAs in live ectoderm and mesoderm cells. We verified that this fraction is independent of expression levels (Fig.S1B). The peculiar ectodermal adhesive rings concentrated high amounts of vinculin (Fig.1E), suggesting that these cells were interacting rather strongly with the substrate. We thus compared adhesion to FN by a rotation assay (Fig.1H). Ectoderm cells adhered almost as efficiently as mesoderm cells. This important observation indicated that the known inability of ectoderm cells to spread and migrate on FN was not due, as one may have hypothesized, to lack of efficient cell-matrix adhesion, but rather to an intrinsic property to organize a different type of adhesive structure. We used the same adhesion assay to compare cadherin-based

adhesion, replacing FN with recombinant C-cadherin extracellular domain as the adhesive substrate. Ectoderm cells showed significantly higher cadherin adhesion than mesoderm cells (Fig.1H), consistent with previous measurements<sup>5,12</sup>. Note however that the difference was relatively modest, an observation that became relevant later in this study.

The analysis of small groups of cells showed that the properties of single dissociated cells were directly reflected at the supra-cellular level, each cell type adopting a distinct, highly stereotypic organization (Fig.1C,D): Ectoderm cells formed compact groups; they still emitted blebs, but exclusively along the edge of the group (Fig.1C). Cells did form some protrusions that crawled under adjacent cells, but typically in an inwards orientation (Fig.1C', yellow concave arrows). The cell group shared a multicellular vinculin/paxillin ring constituted by the juxtaposition of partial rings formed by the individual cells (Fig.1C', arrowheads). On the contrary, mesoderm cells formed widely spread groups with numerous lamellipodia. Both peripheral and internal lamellipodia were oriented outwards (Fig.1D', white and yellow concave arrows). FAs were aligned along the outward direction of the expanding protrusions (arrowheads).

This characterization highlighted deep intrinsic differences between ectoderm and mesoderm cells, which resulted in very different morphologies and in distinct adhesive structures. These correlated well with their all or none migratory capabilities, while differences in matrix and cell-cell adhesion were not as striking. Lastly, the properties observed for isolated cells readily translated into diametrically opposed collective organizations, compacted for ectoderm, expanded for mesoderm.

### **Inhibition of Rock induces mesoderm-like spreading and migration of ectoderm cells**

Ectoderm cells have intrinsically higher myosin-dependent cortical tension than mesoderm<sup>5</sup>. This high tension is reflected in cells plated on FN through their blebbing and by a stronger accumulation of cortical myosin light chain (MLC) (suppl. Fig.S2A-C), as well as in the whole embryo by a stark difference in levels of phosphorylated MLC<sup>13</sup>. We therefore hypothesized that differences in actomyosin contractility could be responsible for the distinct properties of ectoderm and mesoderm with respect to their spreading and migratory capabilities. Rho-kinases (Rock) are important myosin activators. In both ectoderm and mesoderm cells, Rock1 and Rock2 are concentrated along the free cell cortex (suppl. Fig.S2D-K, arrowheads), but present only at low levels at sites of cell-matrix and cell-cell adhesion (suppl. Fig.S2D-K, arrows), consistent with a major role in controlling cortical tension.

We tested the effect of a short-term acute Rock inactivation on ectoderm cellular behaviour using two specific chemical Rock inhibitors, Y27632 and H1152. The effect of these inhibitors on single ectoderm cells plated on FN was spectacular: Cells almost instantaneously stopped blebbing, and within minutes started to spread, emit lamellipodia, and migrate (Fig.2A-B, suppl. Movie 3). These changes were quantified by monitoring the increase in cell surface area (Fig.2E and S2L), the modification of cell morphology (Fig.2F), and by tracking migration (Fig.2G). In all these aspects, Rock inhibition appeared sufficient to induce a dramatic transformation of ectoderm cells into mesoderm-like cells. Similarly, Rock inhibition caused groups of ectoderm cells (Fig.2C,D, suppl. Movie 4) to adopt the typical expanding configuration of mesoderm groups (compare to Fig.1D). The matrix adhesive structures were completely reorganized during this transition: the vinculin ring was disassembled, often starting asymmetrically, coinciding with extension of a protrusion and formation of classical FAs (Fig.2D for a group, also seen in A-C). Note that the supracellular organization of cell groups was also reflected during this transition, with the coordinated asymmetric disassembly of the vinculin ring and the formation of protrusions extending over the entire group (Fig.2C,D, suppl. Movie 4). This

observation further emphasized the congruence between single cell and collective behaviours. Importantly, the rapidity of the changes caused by the inhibitors (Fig.2E and suppl. Fig.S2L) clearly reflected a direct effect and excluded the involvement of transcriptional processes and changes in cell fate.

We also evaluated the effect of Rock inhibition on adhesion (Fig.2H). Rock inhibitors significantly increased adhesion of both ectoderm and mesoderm on FN. They also increased adhesion on cadherin for mesoderm, without a detectable change for ectoderm. In stark contrast, the MLCK inhibitor ML7 potently inhibited adhesion of both tissues, on both FN and cadherin substrates (Fig.2H). We concluded that both cell-matrix and cell-cell adhesions require MLCK activity, but not Rock activity. The latter, on the contrary, appears to act antagonistically to adhesion, which is precisely the expected impact of tension of the cell cortex, where Rock1/2 localize (suppl. Fig.S2D-K). Together, these experiments support our initial hypothesis, pointing towards cortical Rock activity as a gatekeeper that prevents ectoderm from migrating. This model would predict that mesoderm cells should have acquired mechanisms to downregulate cortical contractility in order to spread and migrate.

### **Two Rho antagonists, Rnd1 and Shirin, are essential for mesoderm migratory and adhesive properties during gastrulation**

The most parsimonious scenario that could account for the decreased myosin activity, lower cortical tension and high motility of mesoderm was that this tissue expresses negative regulators of the Rho-Rock pathway. We searched through the *Xenopus laevis* developmental gene expression database (Xenbase<sup>14</sup>) for putative regulators expressed at the onset of gastrulation, and determined by qPCR their relative transcript levels in ectoderm and mesoderm. Two candidates, Rnd1 and Shirin, stood out as being significantly enriched in the mesoderm (Fig.3A). Rnd1 is a small GTPase that antagonizes RhoA through activation of ArhGAP35/p190B-RhoGAP, and is implicated in the control of cell-cell adhesion<sup>15</sup>. Shirin/Dlc2/Stard13/ArhGAP37 is a RhoGAP, that has been associated with various functions, such as migration, adhesion and cell division<sup>16</sup>. The potential role of these two regulators in the migratory properties of the mesoderm had not yet been addressed.

Injection of specific morpholino antisense oligonucleotides (MOs) targeted against Rnd1 or Shirin mRNAs yielded severe gastrulation phenotypes (suppl. Fig.S3A-D), with virtually full penetrance (suppl. Fig.S3E,F). In both cases, the dorsal blastopore lip was strongly reduced or missing altogether (suppl. Fig.S3A-D,E). The internal morphology was similarly deeply affected, revealing a block of mesoderm involution (suppl. Fig.S3A'-D' and F). Importantly, while mesoderm morphogenesis was dramatically impaired, the ectodermal blastocoel roof became as thin as in control embryos, indicating that epiboly, another key morphogenetic movement during gastrulation, proceeded normally. While there were differences between the detailed phenotypes of the two knockdowns, their analysis was of little informative value toward understanding the underlying mechanisms. We thus went on to investigate the Rnd1 and Shirin loss-of-function phenotypes at the cellular level, starting with the analysis of single dissociated cells. Rnd1MO and ShiMO had drastic effects: most injected mesoderm cells failed to spread on FN and often showed blebbing (Fig.3B-D, suppl. Movie 5, quantification in Fig.3F). Their migration was significantly decreased compared to control mesoderm (Fig.3G). Both adhesion on FN and adhesion on cadherin were also significantly impaired (Fig.3H). Specificity of the Rnd1 and Shirin MOs was demonstrated by rescue of spreading and migration upon expression of YFP-Rnd1/YFP-Shirin (suppl. Fig.S4A-D). Moreover, spreading and migration were also rescued by Rock inhibition, demonstrating that indeed Rnd1 and Shirin act upstream of Rock (suppl. Fig.S4A-D).

Beyond these shared effects, we observed differences between Rnd1MO and ShiMO cellular phenotypes. Rnd1MO cells almost completely lacked detectable vinculin-positive FAs (Fig.3C,E), while vinculin distribution in ShiMO cells was heterogeneous (Fig.3E): Some ShiMO cells still harboured classical FAs, others had none, and others started to assemble peripheral concentric FAs strikingly reminiscent of the rings observed in ectoderm cells (Fig.3D). A closer look at migration brought further interesting insights. So far, we had compiled the average migration speed of all cells, independently of their morphology (Fig.3G). In order to better understand the cause of the decreased migration, we analyzed the speed of each category of cells (suppl. Fig.S4E). While the overwhelming majority of wild type mesoderm cells had a spread morphology, other types could be found at low frequency, which allowed us to confirm that the morphology correlated with migration: Spread cells showed the highest speed, while round cells (with or without blebs) showed the lowest. Nevertheless, round and blebbing mesoderm cells were still faster than ectoderm cells ( $1\mu\text{m}/\text{min}$  versus less than  $0.3\mu\text{m}/\text{min}$ ), indicating that, even for this typical “immobile” morphology, mesoderm cells remained capable of some migration. RndMO mesoderm cells showed an identical profile to control mesoderm throughout all categories (suppl. Fig.S4E). We could conclude that the lower average speed of RndMO cells directly reflected their switch from spread to round morphology (Fig.3F). The profile was different for ShiMO: We calculated that the migration speed was significantly decreased by knockdown of Shirin for all morphological categories (suppl. Fig.S4E), implying that ShiMO, in addition to causing a shift in morphology, had also a separate impact on motility. These data thus further argued for a differential role of the two regulators.

In summary, the specific activation of Rnd1 and Shirin expression in mesoderm cells appears absolutely required for mesoderm involution, controlling cell spreading, motility and adhesion, accounting for the predicted pro-migratory effect of downregulation of the Rho-Rock pathway. However, the loss-of-function phenotypes clearly differed in several aspects, indicating that Rnd1 and Shirin had distinct activities.

### **Expression of Rnd1 and Shirin confer ectoderm with mesoderm-like migratory properties**

Next, we tested the effect of overexpressing Rnd1 or Shirin in ectoderm cells, with the rationale that they may reproduce the transition toward a mesoderm-like phenotype observed upon Rock inhibition. Indeed, both Rnd1 and Shirin induced remarkable changes in ectoderm cells: the frequency of blebs was strongly decreased, and a significant number of cells spread on FN, extended protrusions (Fig.4B-E,G), and became motile (Fig.4H,I, suppl. Movie 6). Thus, either of these components was indeed capable to drive ectoderm cells into a migratory mode.

The effects of Rnd1 and Shirin again had distinct characteristics: Shirin was extremely potent at inducing cell spreading and formation of protrusions (Fig.4D,E,G), while Rnd1-expressing cells remained more compact (Fig.4B,C,G). Conversely, Rnd1 had a higher pro-migratory activity (Fig.4H and suppl. Fig.S5). In fact, high Shirin expression caused cells to “over spread” (Fig.4E), which became detrimental to migration (Fig.4H”). In terms of vinculin localization, most Rnd1 and Shirin expressing cells lacked ring structures, and did not show any detectable vinculin accumulation at the substrate interface. However, FA-like structures could be observed in cells expressing moderate levels of Shirin (Fig.4D, arrows). Note that neither Rnd1 nor Shirin expression led to detectable changes in adhesion on FN (Fig.4J). In conclusion, these experiments showed that both Rnd1 and Shirin could induce spreading and migration, but each expressed this property in a slightly different manner, further supporting overlapping yet diverging activities.

## Rnd1 and Shirin modulate cell surface tension and adhesiveness

To verify the effect of Rnd1 and Shirin on cortical contractility, we analyzed isolated cell doublets. In this simple system, the geometry of contact vertices directly reflects the balance of the forces exerted along the three interfaces, i.e. the cortical tensions along free edges ( $C_{t_A}$  and  $C_{t_B}$ ) and the contact tension  $T_{AB}$ <sup>5,17,18</sup>(Fig.5A).  $T_{AB}$  is the sum of the two cortical tensions along the contact interface ( $C_{t_A}'$  and  $C_{t_B}'$ , which are lower than  $C_{t_A}$  and  $C_{t_B}$ ) and of the negative contribution due to cell-cell adhesion (see Material and Methods). Heterotypic doublets made of a wild type ectoderm cell and a cell expressing Rnd1 or Shirin tended to be asymmetric, reflecting differences in their cortical tension (Fig.5B-I). The asymmetry was particularly strong for Shirin: The heterotypic interface was systematically concave, with the Shirin-expressing cell engulfing the wild type cell to various degrees (Fig.5H,I). We calculated that Ct was decreased about two folds in Shirin-expressing cells (Fig.5J). Rnd1 caused a more modest but significant reduction of about 10%. As comparison, we had previously shown that mesoderm cortical tension was about 2-3 folds lower than ectoderm<sup>5</sup>. Doublet geometry also allowed us to compare the relative contact tensions (relT), which was significantly decreased by both Rnd1 and Shirin (Fig.5K). Since cell-cell adhesion is largely dictated by the reduction of cortical tension along the contacts<sup>18-20</sup>, this reduction can be used to express a relative “adhesiveness”,  $\alpha$ , an absolute value that stands from 0 (no adhesion) to 1 (maximal adhesion)<sup>20</sup>(see Material and Methods). Interestingly,  $\alpha$  dropped quite significantly upon Shirin expression, but not Rnd1 expression (Fig.5L). This conclusion was supported by our adhesion assay, which showed that cadherin adhesion was significantly weakened by Shirin, but not by Rnd1 (Fig.5M). In summary, these measurements confirmed that both Rnd1 and Shirin repressed cortical tension, although to different extents. The stronger effect of Shirin explained why Shirin-expressing cells spread at higher frequency and more extensively (Fig.4). From the comparison of the effects of Rnd1 and Shirin on tension (Fig.5J) and on cell spreading (Fig.4G), we can extrapolate that a ~20% reduction in cortical tension may be sufficient to allow ectoderm cells to start to elongate and spread. Rnd1 and Shirin also differed in their impact on adhesiveness. In the case of Rnd1, the decrease in free surface Ct was apparently better compensated by the concomitant decrease in contact tension T, thus maintaining stronger cell-cell adhesion than Shirin.

## Overlapping but distinct subcellular localization of Rnd1 and Shirin

In order to gain additional insights in Rnd1 and Shirin properties in these embryonic cells, we set to examine their subcellular localization. In the absence of adequate antibodies, we used the distribution of YFP fusion constructs as a proxy (Fig.6). In the *Xenopus* embryo, titration of injected mRNA allows the expression of low levels of these fluorescent constructs, and to verify that subcellular patterns are reproducible even at the lowest detectable levels. For Shirin, because of the potent activity of RhoGAPs, even when expressed at low levels, we used a GAP-deficient R488A mutant (mShi) in order to visualize the subcellular distribution with minimal impact on the cell phenotype.

Rnd1 was homogeneously distributed along the cell cortex, both on the ventral side (Fig.6A') and at free cell edges (Fig.6A''), but significantly accumulated at cell-cell contacts (Fig.6A'''). We measured a more than two-fold enrichment at contacts, which is comparable to cadherin accumulation (Fig.6C). mShi also localized to the cell cortex, but, unlike Rnd1, it did not accumulate at cell-cell contacts (Fig.6B'',C). Instead, it formed prominent clusters on the ventral side of protrusions (Fig.6B,B',D,D'). Many of these clusters perfectly colocalized with vinculin FAs (Fig.6D). Wild type Shirin showed a very similar distribution, with the same characteristic ventral clusters (Fig.6E). However, wild type Shirin had a

strong impact on vinculin-positive FAs, which were largely excluded from the Shirin-rich regions of the protrusions and confined to the edges (Fig.6E). We also examined the protrusions induced by Shirin expression in ectoderm cells. The organization of these protrusions was similar to that of mesoderm protrusions, with accumulation of clustered Shirin and confinement of vinculin to the periphery (Fig.6F). Note that in both ectoderm and mesoderm, a Shirin cluster was often found at the proximal end of FAs (arrowheads). In cases of ectoderm cells that had only undergone an incomplete mesoderm transition (Fig.6F), we could detect Shirin lining the inner side of the remnants of the vinculin ring (white and orange arrowheads). One could conclude that Shirin is not only preferentially localized to protrusions, but more specifically targeted to FAs. While inactive Shirin accumulates at these structures, expression of wild type Shirin appears to “clear” vinculin from protrusions, consistent with its reported function in FA disassembly<sup>16</sup>. However, the presence of numerous FAs in non-manipulated mesoderm cells indicates that the normal function of endogenous Shirin is to moderate rather than to remove FAs altogether.

Most strikingly, the sites of Rnd1 and Shirin enrichment, respectively at cell-cell contacts and in ventral protrusions, coincided with the two prominent regions where Rock1/2 were at their lowest level (suppl. Fig.S2). Together with the functional data, these observations suggested that both regulators contributed to the downregulation of Rock-dependent cortical tension along free cell edges, while their complementary specific enrichments fulfill distinct functions at cell contacts: The ventral pool of Shirin would promote lamellipodium extension and keep tension at FAs under control, while Rnd1 would downregulate tension at cell-cell contacts, accounting for its ability to maintain cell-cell adhesiveness (Fig.5).

### **Rho/Rock regulation affects collective migration of ectoderm and mesoderm tissue explants.**

We extended our analysis to tissue-scale dynamics by investigating collective cell migration. For this purpose, we dissected tissue explants, let them heal, and then tested them for their ability to spread on FN for about 3 hours. Note that under these conditions, tissue behaviour depended on the ability of both cell types to migrate on the FN substrate and to rearrange within the explant. In this assay, wild-type ectoderm explants did not spread on the substrate, but often further compacted after plating (Fig.7A, suppl. Movie 7). In contrast, wild-type mesoderm explants quickly began to expand (Fig.7E, suppl. Movie 11). Strikingly, however, their expansion was repeatedly interrupted by rapid, large scale contractions (Fig.7E; red arrowheads, trace in Fig.7I). Mesoderm explants thus reached an apparent “steady-state” mode of alternating spreading and contraction, with an average maximal expansion 2 to 2.5 fold their initial size (Fig.7J,L). This behavior suggested that mesoderm spreading was limited by internal tension. Consistently, treatment of mesoderm with Y27632 completely abolished the retraction phases, leading to a smooth and broader expansion (Fig.7F,I,J,K, suppl. Movie 12). Y27632 also induced spreading of ectoderm explants (Fig.7B,J,K, , suppl. Movie 8). Note that, at later time points (> 2hrs), a small proportion of wild type ectoderm explants also started to spread (Fig.7J, suppl. Fig.S6), consistent with rare cases of spreading and migration of single ectoderm cells (Fig.2J). The behaviour of ectoderm and mesoderm tissues and the response to Rock inhibition were highly reminiscent of the behaviour of single cells (Fig.2), further emphasizing the connection between the cell autonomous characteristics and the tissue properties.

Expression of either Rnd1 or Shirin induced extensive spreading of the ectoderm explants (Fig.7C,D,L,M). However, each regulator caused a distinct mode of spreading. Rnd1-expressing explants, after a delay, rapidly spread while remaining very compact (Fig.7C, suppl. Movie 9), while

explants expressing Shirin became looser as they spread and partly disintegrated with numerous single cells migrating individually (Fig.7D, suppl. Movie 10). The dispersive action of Shirin is consistent with its negative effect on cell-cell adhesiveness (Fig.5J,K'). The trends observed in ectopically expressing ectoderm were mirrored by the behaviour of depleted mesoderm explants. Shirin MO strongly decreased spreading (Fig.7H,N,O, suppl. Movie14), even though cycles of spreading and contraction still occurred (Fig.7H; red arrowheads). In contrast, Rnd1MO caused two distinct phenotypes, depending on the embryo batch: About one third of the Rnd1MO mesoderm explants failed to spread. A majority of explants, however, spread quite extensively in an unusual way (Fig.7G,N,O, suppl. Movie 13): After a slow initial phase, rapid expansion coincided with loss of cohesion among cells migrating on the matrix. This behaviour is clearly reminiscent of cell dissemination observed in Shirin-expressing ectoderm (Fig.7D), suggesting that, in the absence of Rnd1, mesoderm behaviour was dictated by the dispersive activity of Shirin.

### **Effect of Rock inhibition and Rho regulators on tissue physical properties**

To study global effects on physical properties of these tissues, we performed stress-relaxation experiments using the micropipette aspiration technique (MPA). While the actual properties of tissues are quite complex, they can be modelled as viscoelastic materials, where the “elastic” component corresponds to short-term tissue behavior (determined by cortical tension and cell viscoelasticity), while the viscous component reflects the ability of the cells to actively rearrange within the tissue. In an MPA experiment, the initial fast deformation phase is dominated by the short-term properties, and the slower subsequent phase by the long-term properties (“viscosity”). When the pressure is reset to zero, the aspirated portion of the explant will retract due to tissue surface tension (TST), which tends to restore the original spherical shape<sup>21,22</sup>. Stiffness and viscosity of the tissue offer resistance to the retraction, determining again a fast and a slow response. This model enables estimation of both tissue viscosity and TST based on the slopes of the slow viscous phases of aspiration and retraction (see Materials and Methods)<sup>21,22</sup>. In addition, we have also quantified the initial fast deformation, as an indicator of the short-term “stiffness” of the tissue.

We observed clear differences in the behaviour of ectoderm and mesoderm explants (Fig.8A,B, , suppl. Movies 15 and 16). During the initial fast phase, mesoderm explants were aspirated significantly deeper in the pipette (Fig.8A',B',D). Viscosity calculated from the slow phases was also significantly lower for the mesoderm (Fig.8E), while TST was only slightly weaker (Fig.8F), in agreement with previous estimates<sup>17</sup>. Thus, mesoderm appears to be softer and more fluid than ectoderm, but maintains nevertheless a relatively high global tension. Different manipulations of the ectoderm gave distinct phenotypes (examples in Fig.8C, quantification in Fig.8D-I): Y27632 treatment strongly decreased both viscosity and TST of ectoderm, but did not impact on the initial fast aspiration phase. Shirin expression strongly impacted on all parameters, indicating that the tissue had become softer, more fluid, and less cohesive. On the other hand, TST was the sole parameter significantly decreased by Rnd1, stiffness and viscosity remained largely unaffected. These results are in agreement with the cell doublet measurements and with the explant spreading data. Altogether, our data show that while mesoderm properties can be approximated as the result of a global decrease in Rock-dependent contractility, they are best accounted for by distinct actions of Rnd1 and Shirin. The former mostly operates on TST by moderating cortical tension while preserving cell-cell adhesion, while the latter stimulates tissue fluidity and dispersion by dampening both cortical tension and adhesiveness.

## Discussion

Ectoderm and mesoderm cells show diametrically opposed organizations in terms of cytoskeletal organization and adhesive structures, which explains their distinct migratory capabilities at both the single cell and tissue level. Yet we could surprisingly easily convert ectoderm into a migratory, mesoderm-like tissue, by simply tuning down contractility via the Rho-Rock pathway. In fact, even non-manipulated ectoderm is capable, at low frequency, of spontaneous spreading and migration (Fig.2J and suppl. Fig.S6). An important conclusion is that the ectoderm is not irreversibly locked into a non-migratory configuration, but is actively maintained in a low dynamic state by its high contractility. Reciprocally, by targeting the mesoderm-specific Rho negative regulators Rnd1 and Shirin, we could make mesoderm cells at least partly revert to a low-migratory, blebbing, ectoderm-like state. Quite remarkably, this reversion could go so far as to reproduce the characteristic concentric organization of adhesive structures (Fig.3D). These observations suggest that the seemingly deep morphological and behavioural dissimilarities between the two cell types derive from relatively simple molecular differences.

The transition from a cohesive to a dispersive state is reminiscent of the maturation of pre-migratory precursors into migratory neural crest cells that occurs a few hours later<sup>23</sup>. In the neural crest model, the process is driven by a switch from E-cadherin to N-cadherin expression, leading to a shift from inwards to outwards protrusive activity, analogous to what we observe in gastrula tissues (Fig.1C,D)<sup>23</sup>. In this study, however, we find that the mesoderm transition seems to rely on a direct modulation of the cytoskeleton by expression of two negative regulators of RhoA.

Our study highlights a fascinating property of the mesoderm. Despite the high migratory activity of its cells, both as single cells and within the tissue, the tissue is nevertheless rather cohesive and contractile (Fig.7), which is also reflected by the fact that global tensile and viscous properties of this tissue are only marginally lower than those of the ectoderm (Fig.8), as previously noted by Winklbauer and colleagues<sup>17,24</sup>. Thus the ectoderm to mesoderm transition can be viewed as a motility switch, rather than a classical solid to fluid state transition. The fact that the mesoderm does not simply become “liquid” is to be expected, as without sufficient cohesiveness, it could neither generate nor withstand the significant forces that are involved in gastrulation movements<sup>25</sup>.

Note that the viscosity and TST values obtained with the aspiration technique differ significantly from those reported by Winklbauer and colleagues<sup>17,24</sup>. This difference likely reflects the different techniques used, and the different situations that were addressed: Previous work determined the properties of tissue explants through their global deformation under the sole influence of gravity, while we challenged the capacity of the tissues to resist local stress. Differences in “apparent” physical values have to be expected, considering that the cytoskeleton and cell adhesion are likely to behave differently under different stress conditions, and that cells are capable of active reactions that can rapidly and deeply modify these structures and thus tissue rheology. Thus, these estimates must thus be considered as relative values, valid under specific experimental conditions. They are nevertheless highly informative about the properties of tissues and the influence of molecular manipulations. Along the same lines, the spreading assay (Fig.7) tests yet another situation, as spreading is controlled by the balance between the internal properties of the tissue (such as cell-cell adhesion, cortical tension, intercellular motility), and the capacity of cells to spread, adhere and migrate on extracellular matrix. We believe these various assays provide complementary approaches to unravel the mechanisms underlying morphogenetic processes.

This study implicates the Rnd1 - Shirin pair as a key regulator of the ectoderm to mesoderm transition. Rnd1 and Shirin MO embryonic phenotypes are extremely strong and penetrant, demonstrating an absolute requirement of these molecules for mesoderm movements. At the tissue and cell level, Rnd1 and Shirin fulfill common as well as distinct complementary functions. They both promote mesoderm motility, as demonstrated by the decreased single cell migration in Rnd1 MO and Shirin MO mesoderm, which is perfectly mirrored by induction of single cell migration and of explant spreading in the gain-of-function experiments. Their complementary functions were evident in the tissue spreading assay, where the hybrid phenotype of Rnd1 MO mesoderm was particularly informative. Indeed, while the initial slower spreading was consistent with the contribution of Rnd1 in decreasing contractility and promoting motility, the subsequent emergence of a strong dispersive behaviour revealed the underlying Shirin activity, which is otherwise counterbalanced by Rnd1 in the wild type mesoderm. Although these two regulators need to be further characterized, their doppelgänger nature is consistent with the overlapping yet partly complementary subcellular localizations. Thus, their global cortical pools are probably responsible for decreased cell cortical tension, spreading and migration, while their sites of accumulation at protrusions for Shirin and at cell contacts for Rnd1 are consistent with their opposite effects on adhesiveness and tissue cohesion. The dual function of these regulators may also explain some less intuitive phenotypes, in particular the decreased cadherin adhesion for Shirin MO mesoderm cells, which most likely results from an imbalance in cellular tensions under these artificial conditions. Note that we also expect the input of additional components on the contractile and adhesive properties of these tissues, which remain to be identified.

The pro-migratory activity of both Rnd1 and Shirin uncovered here may seem at odds with the traditional view of Rnd1 and the Dlc1,2,3 family, to which Shirin belongs, which presents them as inhibitors of migration and as suppressors of invasion<sup>16,26</sup>. Our results are also inconsistent with earlier reports of an anti-adhesive role for Rnd1 in *Xenopus*<sup>15,27</sup>. However, it is now clear that these molecules can have opposite effects depending on the cell type and the context<sup>16,26</sup>, which is expected considering the multiple effects of RhoA-dependent contractility and the intricacy of its regulation. Note that the ability of Rnd1 to stimulate both migration and cohesion is reminiscent of the properties of EpCAM, a cell membrane protein that also acts as an indirect inhibitor of myosin contractility, although through a completely different pathway<sup>28,29</sup>. These types of regulators must have in common the ability to repress at the same time global cortical tension, accounting for their pro-migratory activity, and tension at cell-cell contacts, thus maintaining the proper force balance that insures tissue cohesiveness<sup>17,18</sup>.

Obviously additional regulatory mechanisms are expected to fine tune the tissue properties in order to achieve the perfectly coordinated ballet of gastrulation movements. For instance, Rnd1 interactors were reported to modulate its function in the mesoderm<sup>27,30</sup>. We must stress, however, that both Shirin and Rnd1 are sufficient on their own to induce the distinct modes of migration described in this study, as shown unambiguously by the effect of their ectopic expression on single ectoderm cells and tissue explants. The cooperation of Rnd1 and Shirin/Dlc2 in enabling mesoderm involution provides an example of how different cytoskeletal regulators may be used to tune tissue behaviour. It will be important to see if the same molecules, or similar pairs of rivals contribute to other processes involving collective migration.

## Materials and methods

### Embryo preparation and injection

Plasmids and morpholino oligonucleotides (Genetools LLC) are listed in Tables S1 and S2 in the supplemental information section. mRNAs were synthesized according to manufacturer instructions (mMessage mMachine kit, Ambion). MOs and mRNAs were injected animally in the two blastomeres of 2-cell stage embryos for ectoderm targeting, or equatorially in the two dorsal blastomeres of 4-cell stage embryos for mesoderm targeting, at amounts listed in Tables S1 and S2.

### Chemicals

Y2762, H1125 and ML7 were from Millipore and Enzo Life Sciences.

### Microdissections and cell dissociation

All dissected explants and cells were taken either from the inner layer of the ectodermal animal cap or from the anterior mesoderm at stage 10.5, except for the MO experiments, in which case the mesoderm was dissected from the dorsal lip at stage 10+, i.e. before involution. Dissections were performed in 1xMBSH (88mM NaCl, 1mM KCl, 2.4mM NaHCO<sub>3</sub>, 0.82mM MgSO<sub>4</sub>, 0.33mM Ca(NO<sub>3</sub>)<sub>2</sub>, 0.33mM CaCl<sub>2</sub>, 10mM Hepes and 10 µg/ml Streptomycin and Penicillin, pH 7.4. Single cells were dissociated in alkaline buffer (88mM NaCl, 1mM KCl and 10mM NaHCO<sub>3</sub>, pH = 9.5)<sup>13</sup>. All subsequent assays were performed in 0.5xMBSH buffer, at room temperature (23°C).

### Confocal microscopy

Glass bottom dishes (CellVis) were coated for 45min with 10µg/ml bovine fibronectin (Sigma-Aldrich) followed by blocking with 5mg/ml bovine serum albumin. Dissociated cells from embryos expressing various fluorescent fusion proteins were plated on the dish and imaged using a spinning disc confocal microscope (Dragonfly, Andor), mounted with two EMCCD cameras (iXon888 Life Andor) for simultaneous dual color imaging, with a 60x objective (Apo lambda, 1.4 NA) and the Fusion acquisition software (Andor). Images were deconvoluted using Fusion software (Andor) and further analyzed using ImageJ.

### Image quantification

All image quantification of confocal images was performed using ImageJ software.

Vinculin-Cherry enrichment was measured on maximal projections of 2 to 3 0.25µm-thick z stacks encompassing the ventral cell surface. A mask was produced to extract the brighter signal of “clustered” vinculin-Cherry corresponding to focal adhesions. The total fluorescence intensity within this mask was divided by the total fluorescence intensity to the whole ventral surface of the cell, after background subtraction.

Relative cortical and contact enrichments of MLC-Cherry, Cadherin-dTomato, Rnd1-YFP and Shirin-YFP were obtained by measuring the average fluorescence intensity of line scans manually drawn along free cell edges or along cell-cell contacts, as well as the intensity in the cytoplasm immediately adjacent to the cell periphery. After background subtraction, the “cortical” enrichment was calculated as cell edge (or cell contact)/cytoplasm.

## Migration assay

Dissociated cells were plated on fibronectin-coated glass bottom dishes and left to adhere for 45-60min, then imaged every 2.5min for 100-170min using a bright field inverted Olympus IX83 microscope (10X UPFLN 0.3NA PH1 objective) and a scMOS ZYLA 4.2 MP camera. Chemical inhibitors were added after four frames (10min) after the beginning of the time lapse. Addition of the inhibitor was set as time zero. The path of individual cells that did not establish contacts with neighbouring cells was manually tracked using ImageJ software. Average speed corresponds to the average of the speeds calculated between each consecutive time point, within the window frames 10 to 40 (25 to 100min).

## Cell morphology

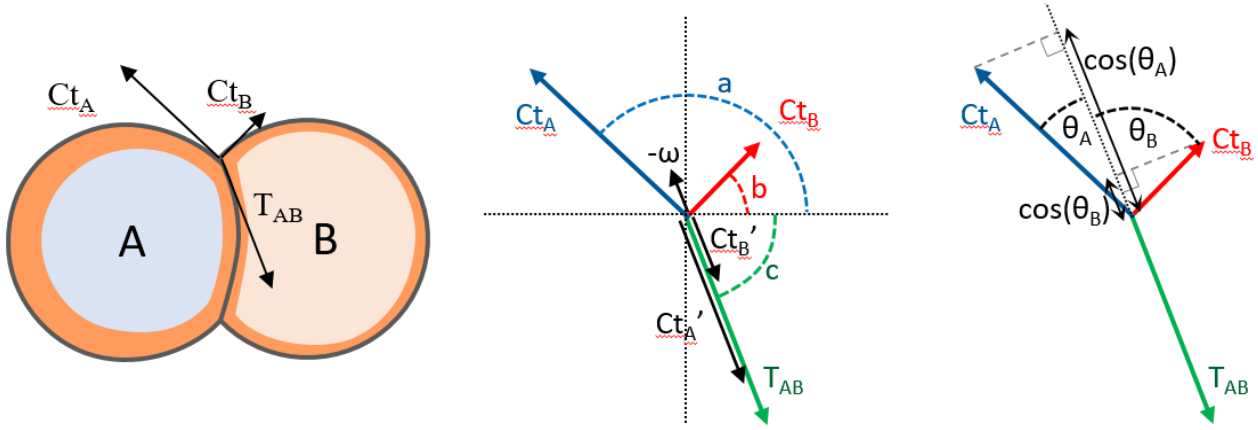
The morphology of each cell was assessed at each time point of the migration assay, and categorized as follows (examples in Fig.2J): Round and blebbing (s), round not blebbing (r), polarized, i.e. elongated but still round-shaped or only partially spread (p), or spread (s). A fifth category included a special phenotype (polarized blebbing, pb), where cells were partially elongated, but had blebs and typically remained anchored to the substrate by one side of the cell. The distribution of morphologies presented in Figs.2I,3J,4G was expressed as the percentage of cells in these five categories observed at time 25'. The speed for each morphological category (suppl. Fig.S3 and Fig.4I') was calculating by extracting the average values for each segment of a track (within frames 10 and 40) during which the cell had adopted a particular morphology.

## Adhesion assay

We used a modified assay based on Niessen et al<sup>31</sup>. 35mm round dishes with a 20mm Ø glass bottom (CellVis) were freshly coated as follows: 1mm Ø circles positioned near the edge of the coverglass, at 8.5mm from the center, were coated with either 10µg/ml fibronectin (Sigma-Aldrich), or with 100µg/ml Protein A followed by 15 µg/µl recombinant C-cadherin extracellular domain fused to human IgG Fc domain, produced and prepared according to<sup>31</sup>. Blocking buffer was as in<sup>31</sup>. Dissociated cells were laid in the coated circles, left to adhere for 45min, and images with an inverted microscope mounted with a 5x objective were collected to determine the initial number of adherent cells. The dishes were then subjected to rotation (10 min at 180rpm for FN, 25min at 200rpm for cadherin), and the fields were imaged a second time to determine the number of cells that had remained attached.

## Calculation of relative tensions for cell doublets

Estimates of relative tensions were based on the principle that the geometry of the cell membranes at cell vertices reflects the equilibrium between the tensile forces exerted by the cell cortices<sup>5,17</sup>. For a doublet formed of cell A and cell B, the equilibrium involved the cortical tensions at the two free cell surfaces ( $C_{tA}$  and  $C_{tB}$ ) and the contact tension at cell-cell interface ( $T_{AB}$ ).  $T_{AB}$  is defined as the sum of the cortical tensions of each cell at the contact ( $C_{tA}'$  and  $C_{tB}'$ ) and of the negative contribution due to cell-cell adhesion ( $-\omega$ ).



The force equilibrium was expressed by two equations:

$$(1) \sin(a) * Ct_A + \sin(b) * Ct_B + \sin(c) * T_{AB} = 0$$

and

$$(2) \cos(a) * Ct_A + \cos(b) * Ct_B + \cos(c) * T_{AB} = 0$$

Angles a, b and c corresponded to the orientation of each force vector. Each of these angles was measured as the tangent to an arc fitted to the cell membrane at the cell vertex<sup>5</sup>.

Based on equations (1) and (2), we could use the three angles to calculate the ratios between the two cortical tensions ( $Ct_A / Ct_B$ ) as well as the ratio between contact tension and each of the cortical tensions<sup>5</sup>.

Adhesiveness  $\alpha$  is defined as the tension reduction at the contacts relative to free surface<sup>20</sup> and can be calculated via the contact angles<sup>20</sup>. We adapted this calculation to asymmetrical doublets, thus

$$(3) \alpha = 1 - T_{AB} / (Ct_A + Ct_B) = 1 - (\cos(\theta_A) + \cos(\theta_B)) / 2$$

### Tissue spreading assay

About 200-300  $\mu\text{m}$   $\varnothing$  explants were prepared by cutting pieces of dissected ectoderm or mesoderm tissues, which were left to heal and round up for 45 min on a non-adhesive agarose coated dish. In cases of treatment with Y2762, the explants were incubated for an additional 45 minutes after healing. The explants were then transferred to fibronectin-coated glass bottom dishes and imaged for 170 min every 2.5 minutes with a 10x objective as described for cell migration. Areas of explants were calculated at each timepoint using CellProfiler (Kamentsky et al., 2011).

### Micropipette Aspiration Assay

MPA was used to measure the viscosity and surface tension of explants as previously described<sup>21,22</sup>. Custom made pipettes with diameters of either 100 or 125  $\mu\text{m}$  with a 15° bend (Sutter Instruments) were passivated with BSA before being used to apply an aspiration pressure of 250 or 220 Pa (depending on the size of the pipette). The aspiration lasted 4-5 minutes, sufficient for the aspiration of the explant to reach a constant velocity; the pressure was then set to zero and the explant was allowed to relax. The pressure was modulated using a Microfluidic Flow Control System and the Maesflow software (Fluigent), and the pipettes were controlled using a PatchStar Micromanipulator and the LinLab2 software (Scientifica). The size of the deformation was automatically calculated using a custom ImageJ macro and used to calculate the rates of aspiration ( $v_{\text{Asp}} = dL_{\text{Asp}}/dt$ ) and retraction ( $v_{\text{Ret}} =$

$dL_{Ret}/dt$ ) of the deformation, which were in turn used to calculate tissue viscosity and surface tension<sup>22</sup>. Briefly, viscosity  $\eta = R_p \Delta P / 3\pi(v_{Asp} + v_{Ret})$  where  $R_p$  is the radius of the pipette and  $\Delta P$  is the applied pressure. Surface tension  $\gamma = P_c / 2(1/R_p - 1/R_0)$ , where  $R_0$  is the radius of curvature of the explant, and  $P_c$  is the pressure that when applied the length of the deformation is equal to  $R_p$ . It can also be calculated from  $P_c = \Delta P v_{Ret} / (v_{Asp} + v_{Ret})$ . Images were acquired every 1 second using a brightfield Zeiss Axiovert 135TV microscope (5x Plan-Neofluar 0.15NA PH1) with a Retiga 2000R camera (QImaging).

## Acknowledgements

We thank Drs. C. Niessen and B. Gumbiner for generous gift of the C-cadherin-Fc-expressing CHO cell line, Dr. K. Cho, F. Spagnoli, A. Brivanlou, N. Kinoshita, and S. Yonemura for plasmids. We thank the Montpellier Rio Imaging platform for technical support. We are grateful to K. Guevorkian and D. Gonzales-Rodriguez for invaluable advice. This work was supported by CIHR grant MOP-130350 to F.F. and P.L., ANR grant ANR-14-ACHN-0004-ICM and by the Labex EpiGenMed to F.F.

## References

1. Keller, R. & Winklbauer, R. Cellular Basis of Amphibian Gastrulation, in *Curr Topics Dev Biol*, Vol. 27 39-89 (Academic Press, Inc., New York; 1992).
2. Wacker, S., Brodbeck, A., Lemaire, P., Niehrs, C. & Winklbauer, R. Patterns and control of cell motility in the *Xenopus* gastrula. *Development* **125**, 1931-1942 (1998).
3. Huang, Y. & Winklbauer, R. Cell migration in the *Xenopus* gastrula. *Wiley interdisciplinary reviews. Dev Biol* **7**, e325 (2018).
4. Winklbauer, R. Cell adhesion in amphibian gastrulation. *Int Rev Cell Mol Biol* **278**, 215-275 (2009).
5. Canty, L., Zarour, E., Kashkooli, L., Francois, P. & Fagotto, F. Sorting at embryonic boundaries requires high heterotypic interfacial tension. *Nature communications* **8**, 157 (2017).
6. Winklbauer, R. & Nagel, M. Directional mesoderm cell migration in the *Xenopus* gastrula. *Dev Biol* **148**, 573-589 (1991).
7. Nakatsuji, N., Smolira, M.A. & Wylie, C.C. Fibronectin visualized by scanning electron microscopy immunocytochemistry on the substratum for cell migration in *Xenopus laevis* gastrulae. *Dev Biol* **107**, 264-268 (1985).
8. Charras, G.T., Coughlin, M., Mitchison, T.J. & Mahadevan, L. Life and times of a cellular bleb. *Biophys J* **94**, 1836-1853 (2008).
9. Winklbauer, R. & Keller, R.E. Fibronectin, mesoderm migration, and gastrulation in *Xenopus*. *Dev Biol* **177**, 413-426 (1996).
10. Han, M.K.L. & de Rooij, J. Converging and Unique Mechanisms of Mechanotransduction At Adhesion Sites. *Trends Cell Biol* **26**, 612-623 (2016).
11. Kale, G.R. *et al.* Distinct contributions of tensile and shear stress on E-cadherin levels during morphogenesis. *Nature communications* **9**, 5021 (2018).
12. Briehor, W.M. & Gumbiner, B.M. Regulation of C-cadherin function during activin induced morphogenesis of *Xenopus* animal caps. *J Cell Biol* **126**, 519-527 (1994).
13. Rohani, N., Parmeggiani, A., Winklbauer, R. & Fagotto, F. Variable combinations of specific ephrin ligand/Eph receptor pairs control embryonic tissue separation. *PLoS Biol* **12**, e1001955 (2014).
14. Session, A.M. *et al.* Genome evolution in the allotetraploid frog *Xenopus laevis*. *Nature* **538**, 336-343 (2016).

15. Wuennenberg-Stapleton, K., Blitz, I., Hashimoto, C. & Cho, K. Involvement of the small GTPases XRhoA and XRnd1 in cell adhesion and head formation in early *Xenopus* development. *Development* **126**, 5339-5351 (1999).
16. Braun, A.C. & Olayioye, M.A. Rho regulation: DLC proteins in space and time. *Cell Signal* **27**, 1643-1651 (2015).
17. David, R. *et al.* Tissue cohesion and the mechanics of cell rearrangement. *Development* **141**, 3672-3682 (2014).
18. Winklbauer, R. Cell adhesion strength from cortical tension - an integration of concepts. *J Cell Sci* **128**, 3687-3693 (2015).
19. Maitre, J.L. *et al.* Adhesion Functions in Cell Sorting by Mechanically Coupling the Cortices of Adhering Cells. *Science* **338**, 253-256 (2012).
20. Parent, S.E., Barua, D. & Winklbauer, R. Mechanics of Fluid-Filled Interstitial Gaps. I. Modeling Gaps in a Compact Tissue. *Biophys J* **113**, 913-922 (2017).
21. Guevorkian, K., Colbert, M.J., Durth, M., Dufour, S. & Brochard-Wyart, F. Aspiration of biological viscoelastic drops. *Phys rev letters* **104**, 218101 (2010).
22. Guevorkian, K. & Maitre, J.L. Micropipette aspiration: A unique tool for exploring cell and tissue mechanics in vivo. *Methods Cell Biol* **139**, 187-201 (2017).
23. Scarpa, E. *et al.* Cadherin Switch during EMT in Neural Crest Cells Leads to Contact Inhibition of Locomotion via Repolarization of Forces. *Dev Cell* **34**, 421-434 (2015).
24. Luu, O., David, R., Ninomiya, H. & Winklbauer, R. Large-scale mechanical properties of *Xenopus* embryonic epithelium. *Proc Natl Acad Sci U S A* **108**, 4000-4005 (2011).
25. Keller, R., Davidson, L.A. & Shook, D.R. How we are shaped: the biomechanics of gastrulation. *Differentiation* **71**, 171-205 (2003).
26. Haga, R.B. & Ridley, A.J. Rho GTPases: Regulation and roles in cancer cell biology. *Small GTPases* **7**, 207-221 (2016).
27. Ogata, S. *et al.* TGF-beta signaling-mediated morphogenesis: modulation of cell adhesion via cadherin endocytosis. *Genes Dev* **21**, 1817-1831 (2007).
28. Maghzal, N., Kayali, H.A., Rohani, N., Kajava, A.V. & Fagotto, F. EpCAM Controls Actomyosin Contractility and Cell Adhesion by Direct Inhibition of PKC. *Dev Cell* **27**, 263-277 (2013).
29. Maghzal, N., Vogt, E., Reintsch, W., Fraser, J.S. & Fagotto, F. The tumor associated EpCAM regulates morphogenetic movements through intracellular signaling. *J Cell Biol* **119**, 645-659 (2010).
30. Chen, X., Koh, E., Yoder, M. & Gumbiner, B.M. A protocadherin-cadherin-FLRT3 complex controls cell adhesion and morphogenesis. *PLoS ONE* **4**, e8411 (2009).
31. Niessen, C.M. & Gumbiner, B.M. Cadherin-mediated cell sorting not determined by binding or adhesion specificity. *J Cell Biol* **156**, 389-399 (2002).
32. Fagotto, F., Rohani, N., Touret, A.S. & Li, R. A molecular base for cell sorting at embryonic boundaries: contact inhibition of cadherin adhesion by ephrin/ Eph-dependent contractility. *Dev Cell* **27**, 72-87 (2013).

## Figure legends

### Figure 1. Distinct properties of ectoderm and mesoderm at the cellular level

**A-E) Organization of cell-matrix adhesive structures.** Dissociated *Xenopus* ectoderm (A,C) and mesoderm (B,D) cells expressing vinculin-Cherry (Vin-Che) and membrane-targeted YFP (mYFP) were plated on fibronectin (FN), either as single cells (A,B) or as small groups (C,D) and imaged live by spinning disc confocal microscopy. y: autofluorescence of yolk platelets. Ventral: ventral z plane close to the glass. max p: Maximal z projection.

A) Ectoderm cells do not spread on FN, but adhere to it through a characteristic adhesive ring (A,A', filled arrowheads). They typically form blebs that are continuously pushed around the cell (dashed line with arrow). Right inserts: Orthogonal view (orth) showing the cross-section of the membrane and of the vinculin ring (filled arrowheads). The dashed line underlines the bottom of the bleb.

B) Mesoderm cells spread on FN, and extend multiple lamellipodia. They transiently polarize during their migration, with one protrusion becoming the tail (t), see also time lapse Fig.S1. They form vinculin-positive focal adhesions (FAs, concave arrowheads), generally oriented in the direction of the protrusions (arrows).

C) Ectoderm cells form compact groups, with few protrusions in the center, and numerous blebs at the periphery (dashed lines). External cells emit protrusions under the more central cells (yellow arrows). Individual cells build partial adhesive structures (filled arrowheads), which together form an inter-cellular ring.

D) Mesoderm cells form looser groups, each cell emitting multiple lamellipodia, most of them extending outwards (white and yellow arrows indicate peripheral and internal lamellipodia, respectively), with numerous focal adhesions oriented radially (arrowheads). Panel D' is an enlargement of the upper portion of panel D). Scale bars: A,C,D 10 $\mu$ m; B 20 $\mu$ m; D' 5 $\mu$ m.

E) Quantification of vinculin accumulation at FAs of isolated cells, expressed as Vinc-Che fluorescence concentrated in clusters divided by the total fluorescence along the ventral cortex. The box plot shows the interquartile range (box limits), median (centre line and corresponding value), and min and max values without outliers (whiskers). Statistical comparison using two-sided Student's *t*-test. For all experiments presented in this study, p values are indicated as follows: \*P < 0.05, \*\*P < 0.01, \*\*\*P < 0.001, NS not significant, and a colour code indicates comparison to control to ectoderm (blue) or to mesoderm (red). The numbers in brackets correspond to the number of cells/ number of experiments.

**F) Single cell motility.** Frames of spinning disc confocal time lapse movies. Cells expressed paxillin fused to YFP (Pax-YFP) and membrane Cherry. F) Ectoderm cells are immobile, anchored by their stationary adhesive ring (arrowheads) and bleb (star). Scale bars: F 5 $\mu$ m; F' 20 $\mu$ m. F') Mesoderm cells actively migrate, rapidly remodelling protrusions and FAs (colour-coded arrows and arrowheads indicate successive positions in, respectively, one extending lamellipodium and the retracting tail). White arrowheads: FAs at thin protrusions.

**G) Quantification of single cell migration.**

**H) Adhesion assay.** Dissociated cells were plated on the adherent substrate, either FN or recombinant cadherin-Fc fusion protein, then subjected to rotation. Adhesion is expressed as the percentage of cells remaining adherent after rotation (see Materials and Methods). The column plots show averages and standard deviation of 15 experiments. Two sided Student's *t*-test.

## Figure 2. Inhibition of Rock confers ectoderm cells with mesoderm-like properties

### A-E) Induction of cell spreading and migration by Rock inhibition.

A-D) Confocal imaging of initiation of spreading and migration for single cells (A,B) and small groups of cells (C,D). Rock inhibitors, Y27632 (50 $\mu$ M) and H1125 (1 $\mu$ M) were added at time = 0'. Note that the onset of the transition is not synchronous. In D, the green channel was omitted for better observation of the progressive change in vinculin distribution from the ectoderm ring to classical FAs. Arrows: Nascent protrusions; Filled arrowheads: ring-like adhesion; Concave arrowheads: FAs. Scale bars: 10 $\mu$ m.

E) Measure of area expansion after 50 $\mu$ M Y27632 inhibitor treatment. Average and SD of 107 cells.

**F) Shift in cell morphology.** Cells were classified in morphological subtypes: Round and blebbing (b), round without blebs (r), polarized (p) and spread (s). In wild type conditions, round cells are typically immotile, while polarized and spread cells migrate. A fifth category, named polarized with bleb (pb), includes cells with irregular morphology and blebs. The diagram shows the distribution of wild type mesoderm and ectoderm cells, as well as of ectoderm cells treated for 50min with 10 $\mu$ M or 50 $\mu$ M Y27632 (Y10, Y50) or 1 $\mu$ M H1125 (H). For b and s categories, conditions were compared to control ectoderm by one-way ANOVA followed by Tukey's HSD post hoc test.

**G) Migration speed of Rock-inhibited cells.** Quantification as in Fig.1. Comparison to ectoderm control by one-way ANOVA followed by Tukey's HSD post hoc test.

**H) Opposite effects of Rock and MLCK inhibition on cell adhesion.** Ectoderm and mesoderm adhesion to FN or cadherin was measured after treatment with Rock inhibitors Y27632 (Y, 50 $\mu$ M), H1125 (H, 1 $\mu$ M), or the MLCK inhibitor ML7. Comparison to control ectoderm or mesoderm (five experiments) using pairwise two-sided Student's *t*-test.

## Figure 3. Rnd1 and Shirin are essential for mesoderm spreading and migration

**A) Rnd1 and Shirin expressions are enriched in the mesoderm.** RT-qPCR from dissected tissue.

A) mRNA levels in ectoderm and mesoderm, normalized to homogeneously expressed ODC. 3 to 6 experiments, pairwise one-sided Student's *t*-test.

### B-H) Loss-of-function cellular phenotypes.

B-D) Examples of control morpholino (COMO), RndMO and ShiMO mesoderm cells, expressing Vinculin and mYFP, plated on FN. B-D) Ventral z planes, merged channels; B'-D'') vinculin alone; B''-D'') Maximal z projections. Protrusions are indicated by arrows, FAs by concave arrowheads, vinculin ring by filled arrowheads. Dotted lines highlight the max lateral extension of the cell mass. B) Control spread mesoderm with large protrusions and numerous FAs. t: tail. C) Typical RndMO cell displaying a bulging body (C''', dotted lines) and a small ventral surface with diffuse vinculin (C''', pink line). D) Example of a bulky ShiMO cell with intermediate adhesive structures, including small FAs at short protrusions (arrows) and ectoderm-like partial ring encompassing most of the ventral surface (arrowheads). A bleb is visible in the max projection (D'', dashed line). Scale bars 10 $\mu$ m.

B'''-D''') Schematic diagrams summarizing the general cell morphology and adhesive structures.

**E) Quantification of vinculin accumulation.** Comparison to COMO using pairwise two-sided Student's *t*-test. RndMO cells have little to no detectable vinculin-rich structures. ShiMO cells show high variability (see main text).

**F) RndMO and ShiMO cells show a significant shift in morphology** from spread to round and blebbing cell. Comparison for either of the two categories with corresponding COMO (red asterisks), one-way ANOVA followed by Tukey's HSD post hoc test.

**G) Both RndMO and ShiMO inhibit cell migration.** Grey asterisks: Comparison with double injection RndMO + ShiMO, which significantly enhanced the migration phenotype. One-way ANOVA followed by Tukey's HSD post hoc test.

**H) Inhibition of cell adhesion on FN and on cadherin substrates.** 5 experiments, pairwise two-sided Student's *t*-test.

**Figure 4. Ectopic expression of Rnd1 or Shirin confers ectoderm with mesoderm-like morphological and migratory properties**

**A-G) Effect on cell morphology and vinculin distribution.**

A-E) Examples of ectoderm cells co-expressing Vinc-Che and either mYFP (A, control ectoderm), Rnd1-YFP (B,C) or Shirin-YFP (Shi-YFP, D,E). A) Typical ectoderm cells, with its distinctive vinculin ring (arrows) and two blebs (dashed lines). B) Moderate Rnd1 phenotype: The ventral surface spreads and elongates (concave arrowheads) and is homogenous for vinculin, but the cell remains roundish (contours highlighted by dotted lines), although blebs are absent. C) Stronger Rnd1 phenotype: The cell is flatter and shows a small FA-like vinculin signal (arrow). D) Shirin-expressing cell with prominent lamellipodium and FAs (arrows). E) Shirin-expressing cell with extremely long and disorganized protrusions. Note the absence of the distinctive ectoderm vinculin ring in B-E. Scale bars: 10 $\mu$ m.

F) Quantification of vinculin accumulation. Consistent with the loss of the ring and the paucity of FAs, most of vinculin is homogeneously distributed on the ventral surface.

G) Distribution of morphological subtypes. Both Rnd1 and Shirin cause a strong shift toward spread cells.

**H-I) Effect on cell migration and adhesion**

H) Frames from time laps movies. Examples of Rnd1 and Shirin-expressing ectoderm cells spreading and migrating. The cell in H' spreads extensively, ending with multiple protrusion (black arrowheads) and low motility. Scale bar: 20 $\mu$ m.

I) Quantification of cell migration, as above. Different levels of Rnd1 and Shirin expression were tested (250 and 500pg mRNA for Rnd1, 75 and 150-300pg for Shirin). I') Speed calculated for cells displaying a spread morphology. Rnd-expressing cells show higher migration than wild type or Shi-expressing cells. Statistical comparisons: One-way ANOVA followed by Tukey's HSD post hoc test.

**J) Quantification of cell adhesion on FN.** 5 experiments, pairwise two-sided Student's *t*-test.

**Figure 5. Ectopic expression of Rnd1 or Shirin modulates ectoderm cortical tension and adhesiveness.**

**A) Diagram of an asymmetrical cell doublet**, representing the balance between cortical tensions at free edges  $C_{tA}$ ,  $C_{tB}$  and contact tension  $T_{AB}$ . The orange layer symbolises the actomyosin cortex. The curved cell-cell interface reflects unequal  $C_{tA}$  and  $C_{tB}$  tensions.

**B-I) Examples of homotypic and heterotypic doublets**, imaged by live confocal microscopy. Doublets were made by combining dissociated control ectoderm expressing mYFP (ctrl) and either Rnd1 or Shirin-expressing cells marked with mCherry. Wild type and Rnd1-expressing cells often displayed blebs (dashed lines). Curved interfaces indicative of tensile differences were observed for all combinations, including for homotypic doublets (e.g. panel E), but were most systematically found for heterotypic ctrl-Shirin doublets (H,I). Scale bar: 20 $\mu$ m.

**J-L) Relative tension measurements based on the geometry at cell vertices** (see Material and methods). Note that vertices flanked by a bleb (D and I) were omitted from calculations. H) Ratio between cortical tensions ( $C_{tA}/C_{tB}$ ); I) Relative strength of  $T_{AB}$  compared to control ectoderm-

ectoderm  $T$  arbitrarily set at 1. J) Relative adhesiveness  $\alpha$ . Numbers into brackets: vertices/experiments. Statistical comparison to control doublets using one-way ANOVA followed by Tukey's HSD post hoc test.

**M) Quantification of cell adhesion on cadherin.** 4 experiments, pairwise two-sided Student's  $t$ -test.

### Figure 6. Differential subcellular distribution of Rnd1 and Shirin

A,B) Live confocal microscope images of groups of mesoderm cells co-expressing cadherin-dTomato (Cad-Tom) and either Rnd1-YFP or GAP-deficient mutant ShirinR488A-YFP (mShi-YFP). Both Rnd1 and mShi localize to the cell cortex (concave arrowheads). On the ventral side, mShi is concentrated at protrusions (B', arrows), while Rnd1 is homogenously distributed. Rnd1, but not mShi, is concentrated at cell-cell contacts (flat arrowheads).

C) Quantification of Rnd1 and Shirin at cell-cell contacts, expressed as ratio of the signal intensity at cell-cell contacts divided by twice the signal along free cell edges. Rnd1 is enriched more than two folds at contacts, similar to cadherin. mShi is distributed homogenously along the cell periphery. Comparison Rnd1/mShi to cadherin (red), or mShi to Rnd1 (black) using two-sided Student's  $t$ -test.

D,E) Ventral surface of mesoderm cells co-expressing either mShi or wild type Shirin (wtShi) and Vinc-Che. D) mShi extensively colocalises with vinculin at FAs (white arrowheads in inserts). E) wtShi clusters are present throughout the ventral side of protrusions (arrows). Vinculin-positive FAs are largely confined to the periphery, often colocalized (white arrowhead) or apposed to wtShi clusters (orange and white concave arrowheads).

F,G) Ectopic wtShi in ectoderm cells. F) Detail of a protrusion of a fully spread cell. Similar to mesoderm, the center of the protrusion is occupied by clusters of wtShi and devoid of FAs (arrow). Small FAs are located at the periphery, closely apposed to Shirin clusters (orange and white concave arrowheads). G) Incompletely spread wtShi-expressing ectoderm cells. The left cell has lost its vinculin ring, and a wtShi-enriched protrusion is forming (arrow). The right cell still shows a weak ring lined in the inside by wtShi clusters (orange and white concave arrowheads). Scale bars: 10 $\mu$ m.

### Figure 7. Rho/Rock regulation affects collective migration of ectoderm and mesoderm tissues.

Tissue explants were laid on FN and their spreading was imaged for 170 minutes.

A-D) Control ectoderm, ectoderm treated with 50 $\mu$ M Y27632, and ectoderm expressing Rnd1 or Shirin. Numbers in brackets are number of explants and number of experiments.

E-H) Control mesoderm, mesoderm treated with Y26862, and explants injected with Rnd1 or Shirin MOs. Red arrowheads in E and H indicate areas of large scale retractions (compare 85 and 170min).

I-O) Quantification of explant spreading. After segmentation, the area was calculated for the time course and normalized to the first time point. I) Examples of traces for single explants, illustrating the irregular expansion of mesoderm explants interrupted by retractions. In contrast, expansion of Y26862-treated mesoderm is smooth. J,L,M) Average time course curves with SD for the various experimental conditions. K,M,O) Corresponding relative spreading after 60min and 170min. Statistical comparisons: One-way ANOVA followed by Tukey's HSD post hoc test.

### Figure 8. ROCK inhibition and Rho regulators modulate tissue stiffness, viscosity and surface tension.

Micropipette aspiration was used to measure physical properties of tissue explants. Explants were aspirated into the pipette at constant pressure, then pressure was reset at zero to let the explant retract.

A,B) Examples of aspiration and released of control ectoderm and mesoderm explants. Aspiration pressure was 250 Pa. Pressure was released after 240 sec. Scale bars: 100 $\mu$ m. A',B') Corresponding aspiration and release profiles. The blue double arrows indicate the extent of deformation of the tissue during the first 20 seconds, defined as the fast "passive" phase. The two slow, linear phases of aspiration and release, highlighted in red, were used to calculate viscosity and tissue surface tension. Scale bars: 100 $\mu$ m.

C) Examples of aspiration control ectoderm, ectoderm treated with Y26862, or expressing Rnd1 or Shirin, and control mesoderm. Pressure was 250Pa. Images display the frame corresponding to the deformation 220 seconds after the initiation of aspiration. The colored overlays indicate the distances of deformation respectively during the first fast phase (blue) and during the subsequent slow phase (red). Scale bar: 100 $\mu$ m.

D-I) Calculated parameters: D,G) Length of deformation 20 seconds after initiation of aspiration, encompassing the initial passive phase. E,H) Tissue viscosity calculated from the rates of aspiration and retraction (see Material and Methods). (F,I) Tissue surface tension. Numbers into brackets are number of explants and number of experiments. Statistical comparisons: One-way ANOVA followed by Tukey's HSD post hoc test.

## Supplemental Table S1

### List of mRNA

All plasmids are based on the pCS2+MTYFP vector <sup>32</sup>.

Plasmid	mRNA injected per blastomere at 2 cell stage (pg)
mCherry (membrane-targeted YFP)	50-250
mYFP (membrane-targeted YFP)	50-250
C-cadherin-dTomato	1000
Vinculin-Cherry	125-250
Paxillin-YFP	250
Myosin light chain (MLC)-Cherry	500
Non-muscle myosin heavy chain 2A (NMHC2A)-YFP	1000
Non-muscle myosin heavy chain 2B (NMHC2B)-YFP	1000
Rnd1-YFP	125-500
Shirin-YFP	75-300
ShirinR488A-YFP	75

## Supplemental Table S1

### List of morpholinos

Target	Sequence	Amount/injected blastomere
C-cadherin	CCACCGTCCCGAACGAAGCCTCAT	40ng
Rnd1a	AGTACGGTGGGACAAATCCAACAAC	20ng+
Rnd1b	ACAAGTCCTAATTAAAAGCTCCACG	20ng
ShirinS2a	CTGGCCTCCCATT'TTCCCAGAAAGGT	20ng+
ShirinS2b	GCCTCCCATT'TTCCCAGAGACACGA	20ng

## Legends supplementary figures

**Figure S1** (Related to figure 1)

**A) Mode of mesoderm locomotion.** Consecutive frames from time lapse of mYFP labelled mesoderm cells migrating on FN. The behaviour of the central cell is highlighted: The cell emits one or multiple protrusions (red arrows). One of the protrusions becomes a tail (yellow arrowhead) as the cell stretches toward another direction, and eventually retracts (red arrowheads).

**B) Quantification of accumulation of Vinculin-Cherry in focal adhesions: Linearity between fluorescence levels in focal adhesion and total intensity** (Related to figure 1A-D) Because Vinculin-Cherry expression levels vary from cell to cell, quantification was performed for individual cells by measuring fluorescence in bright clusters (corresponding to focal adhesions) and in the total ventral cell surface (pink on the diagram). The plot shows the average intensity of the ventral surface versus the average intensity in focal adhesions for control mesoderm cells in one experiment, each dot corresponding to a single cell. It shows that accumulation at focal adhesions is proportional to total expression levels over a wide range. Linearity was similarly verified for each experiment.

**Figure S2** (Related to Figure 2)

**A-C) Differential MLC accumulation at the cell cortex.** Ectoderm and mesoderm cells expressing MLC-Cherry (MLC-Che) and mYFP. A) Ectoderm cells show strong accumulation around the cell body (arrows) and part of the blebs (arrowhead). B) Mesoderm cells show irregular cortical MLC, mostly at the concave regions near or between protrusion. C) Quantification of cortical MLC, expressed as the ratio of cortical /cytoplasmic fluorescence intensities. Blebs and protrusions were excluded from the measurements. Statistical comparison using two-sided Student's t-test. Scale bars: A' 5 $\mu$ m, B' 10 $\mu$ m, B'' 5 $\mu$ m.

**D-K) Subcellular localization of Rock1-YFP and Rock2-YFP in ectoderm and mesoderm cells** Selected single planes from live confocal microscopy, either near the glass (ventral), or about 5-10 $\mu$ m above (medial). Concave white arrowheads point at examples of Rock1/2 accumulation. D,E,H,I) Localization relative to the cell cortex and to vinculin-Cherry labelled cell-matrix adhesive structures (red arrowheads). F,G,J,K) Localization relative to cell-cell contacts, marked by cadherin-dTomato (red arrows). D,E) In the ectoderm, Rock1 and 2 have both a cortical localization. Levels are low on the ventral side inside the adhesive ring, but stronger outside of the ring, particularly for Rock2. F,G) Levels are very low at cell-cell contacts. H,I) In the ventral face of mesoderm cells, Rock1 tend to be enriched in the central part, Rock2 at the periphery of the protrusions. Both are low at FAs. They both accumulate at the cortex along cell free edges (medial planes). J,K) Levels are low at cell-cell contacts. Y: autofluorescence of yolk platelets, abundant in mesoderm cells.

**L) Quantification of single ectoderm cell spreading upon H1125 treatment.** Average and SD of 34 cells.

**Figure S3** (Related to Figure 3)

**Loss-of-function whole embryo phenotypes.** 4-cell stage embryos were injected in the dorsal side (d) with a control (COMO), Rnd1 (RndMO) or Shirin (ShiMO) morpholinos. Embryos were fixed and imaged at stage 11. A-C) Examples of typical control, RndMO and ShiMO phenotypes. D) Example of a "partial" phenotype (here ShiMO). A-D) External views from the vegetal pole. Red arrows point to the position of the dorsal blastopore lip of a control embryo, absent in RndMO (B) and ShiMO (C) embryos. D) Partial phenotype, the lip is present but the blastopore has remained widely open compared to control. Note that in many embryos the ventral blastopore is also affected, due to the

diffusion of the morpholinos to the ventral blastomeres before complete separation after the 2<sup>nd</sup> cleavage. A'-D') Sagittally bisected embryos. In a control embryo (A'), the extent of involution (dashed black arrow) can be seen by the position of the tip of the mesendoderm (white arrow) that has moved far away from the blastopore lip (red arrow). B') RndMO embryo lacking any sign of involution. The white arrowhead points to the dorsal edge of the blastocoel cavity (bl), resembling that of a pregastrula embryo. C') Characteristic ShiMO phenotype, with flat blastocoel floor (white arrow) and thicker non-involuting dorsal marginal zone (black arrowheads), both indicative of failed involution. D') Partial involution (white arrow). Yellow arrowheads: thin blastocoel roof, indicative of ectoderm epiboly in all conditions. Scale bars: 200µm. E and F) Score of the penetrance of the gastrulation external and internal phenotype: N, normal embryo; P, partial inhibition, C, complete inhibition. Comparison by one-way ANOVA followed by Tukey's HSD post hoc test.

**Figure S4** (Related to Figure 3)

**A-D) Rescue of Rnd1MO and ShiMO spreading and migration phenotypes.** 4-cell stage embryos were injected in the dorsal side with COMO, RndMO, RndMO + YFP-Rnd1 mRNA (rescue), ShiMO, or ShiMO + YFP-Shirin mRNA (rescue). Dissociated mesoderm cells were plated on FN and time lapse movies were recorded. The fourth condition represents RndMO or ShiMO cells treated with 50µM Y27632 Rock inhibitor (Y). Red, purple and green asterisks: Comparison to COMO, RndMO or ShiMO, respectively. One-way ANOVA followed by Tukey's HSD post hoc test.

**E) Migration speed for different cell morphology categories** (Related to Figure 3) Analysis of data from figure 3K. Red asterisks: Comparison to COMO. one-way ANOVA followed by Tukey's HSD post hoc test.

**Figure S5** (Related to Figure 4)

Histograms showing speed distribution for ectoderm cells expressing Rnd1 or Shirin, compared to wild type ectoderm and mesoderm. Brackets: Range of high speed, comparable to mesoderm, achieved mainly by Rnd1-expressing cells.

**Figure S6** (Related to Figure 7)

Example of ectoderm explant showing late partial spreading, which is only observed beyond the 120min.

## Supplementary Movies

### Supplementary Movie 1

Related to Fig1F. Live imaging of ectoderm cell plated on FN. Red: membrane-Cherry, green: paxillin-YFP. Left: ventral plane, right: Maximal z projection. One frame every 5 minutes for 50min. 60X objective. Scale bar: 10µm.

### Supplementary Movie 2

Related to Fig1F. Live imaging of mesoderm cell plated on FN. Red: membrane-Cherry, green: paxillin-YFP. Ventral plane. One frame every 5 minutes for 50min. 60X objective. Scale bar: 10µm.

### Supplementary Movie 3

Related to Fig.2A. Ectoderm cell treated with 50 $\mu$ M Y27632. Red: Vinculin-Cherry, green: membrane YFP. One frame every 4.5 minutes for 45min. 60X objective. Scale bar: 10 $\mu$ m.

#### **Supplementary Movie 4**

Related to Fig.2C. Group of ectoderm cells treated with 50 $\mu$ M Y27632. Left: ventral plane. Right: Maximal z projection. One frame every 4.5 minutes for 45min. Red: Vinculin-Cherry, green: membrane YFP. 60X objective. Scale bar: 20 $\mu$ m.

#### **Supplementary Movie 5**

Related to Fig.3. Migration of single cells on FN. Examples of control ectoderm, control mesoderm, mesoderm + Rnd1MO, + ShiMO, + ShiMO + 75pg Shirin mRNA (rescue), and + ShiMO + Y27632 treatment. One frame every 2.5 minutes. Bright field, 10x objective.

#### **Supplementary Movie 6**

Related to Fig.4. Examples of migration of ectoderm cells ectopically expressing Rnd1 (250pg mRNA) or Shirin (75pg mRNA). One frame every 2.5 minutes. Bright field, 10x objective.

#### **Supplementary Movie 7**

Related to Fig.7. Wild type ectoderm explant on FN. Merge of bright field and blue fluorescence of Hoechst-labelled nuclei.

#### **Supplementary Movie 8**

Related to Fig.7. Ectoderm treated with Y27632

#### **Supplementary Movie 9**

Related to Fig.7. Ectoderm expressing Rnd1 (250pg mRNA)

#### **Supplementary Movie 10**

Related to Fig.7. Ectoderm expressing Shirin (75pg mRNA)

#### **Supplementary Movie 11**

Related to Fig.7. Control mesoderm

#### **Supplementary Movie 12**

Related to Fig.7. Mesoderm treated with Y27632

#### **Supplementary Movie 13**

Related to Fig.7. Mesoderm + Rnd1MO

#### **Supplementary Movie 14**

Related to Fig.7. Mesoderm + ShiMO

#### **Supplementary Movie 15**

Related to Fig.8. Pipette aspiration of control ectoderm explant

#### **Supplementary Movie 16**

Related to Fig.8. Pipette aspiration of control mesoderm explant